

Depth resolved photothermal OCT detection of macrophages in tissue using nanorose

Amit S. Paranjape,¹ Roman Kuranov,³ Stepan Baranov,^{1,*} Li Leo Ma,²
Joseph W. Villard,³ Tianyi Wang,¹ Konstantin V. Sokolov,¹ Marc D. Feldman,^{3,4}
Keith P. Johnston,² and Thomas E. Milner¹

¹Dept. of Biomedical Engineering, The University of Texas at Austin, Texas 78712, USA

²Dept. of Chemical Engineering, The University of Texas at Austin, Texas 78712, USA

³University of Texas Health Science Center, San Antonio, Texas 78229, USA

⁴South Texas Veterans Health Care System, San Antonio, Texas 78229, USA

*stepan@baranov.su

Abstract: Application of photothermal Optical Coherence Tomography (OCT) to detect macrophages in *ex vivo* rabbit arteries which have engulfed nanoclusters of gold coated iron oxide (nanorose) is reported. Nanorose engulfed by macrophages associated with atherosclerotic lesions in rabbit arteries absorb incident laser (800nm) energy and cause optical pathlength (OP) variation which is measured using photothermal OCT. OP variation in polydimethyl siloxane tissue phantoms containing varying concentrations of nanorose match values predicted from nanoparticle and material properties. Measurement of OP variation in rabbit arteries in response to laser excitation provides an estimate of nanorose concentration in atherosclerotic lesions of 2.5×10^9 particles/ml. OP variation in atherosclerotic lesions containing macrophages taking up nanorose has a different magnitude and profile from that observed in control thoracic aorta without macrophages and is consistent with macrophage presence as identified with RAM-11 histology staining. Our results suggest that tissue regions with macrophages taking up nanorose can be detected using photothermal OCT.

©2010 Optical Society of America

OCIS codes: (170.4500) Optical Coherence Tomography; (170.3880) Medical and Biological Imaging.

References and links

1. J. Aaron, N. Nitin, K. Travis, S. Kumar, T. Collier, S. Y. Park, M. José-Yacamán, L. Coghlan, M. Follen, R. Richards-Kortum, and K. Sokolov, "Plasmon resonance coupling of metal nanoparticles for molecular imaging of carcinogenesis in vivo," *J. Biomed. Opt.* **12**(3), 034007 (2007).
2. P. Diagaradjane, A. Shetty, J. C. Wang, A. M. Elliott, J. Schwartz, S. Shentu, H. C. Park, A. Deorukhkar, R. J. Stafford, S. H. Cho, J. W. Tunnell, J. D. Hazle, and S. Krishnan, "Modulation of in vivo tumor radiation response via gold nanoshell-mediated vascular-focused hyperthermia: characterizing an integrated antihypoxic and localized vascular disrupting targeting strategy," *Nano Lett.* **8**(5), 1492–1500 (2008).
3. M. Longmire, P. L. Choyke, and H. Kobayashi, "Clearance properties of nano-sized particles and molecules as imaging agents: considerations and caveats," *Nanomedicine (Lond)* **3**(5), 703–717 (2008).
4. S. E. Skrabalak, J. Chen, L. Au, X. Lu, X. Li, and Y. Xia, "Gold Nanocages for Biomedical Applications," *Adv. Mater.* **19**(20), 3177–3184 (2007).
5. C. Joo, T. Akkin, B. Cense, B. H. Park, and J. F. de Boer, "Spectral-domain optical coherence phase microscopy for quantitative phase-contrast imaging," *Opt. Lett.* **30**(16), 2131–2133 (2005).
6. M. A. Choma, A. K. Ellerbee, S. Yazdanfar, and J. A. Izatt, "Doppler flow imaging of cytoplasmic streaming using spectral domain phase microscopy," *J. Biomed. Opt.* **11**(2), 024014 (2006).
7. R. Weisleder, "Molecular imaging in cancer," *Science* **312**(5777), 1168–1171 (2006).
8. W. Jiang, B. Y. Kim, J. T. Rutka, and W. C. Chan, "Nanoparticle-mediated cellular response is size-dependent," *Nat. Nanotechnol.* **3**(3), 145–150 (2008).
9. K. Carlson, M. Chidley, K.-B. Sung, M. Descour, A. Gillenwater, M. Follen, and R. Richards-Kortum, "In vivo fiber-optic confocal reflectance microscope with an injection-molded plastic miniature objective lens," *Appl. Opt.* **44**(10), 1792–1797 (2005).
10. G. Mie, "Beiträge zur Optik trüber Medien, speziell kolloidaler Metallösungen," *Ann. Phys.* **330**(3), 377–445 (1908).

11. P. K. Jain, K. S. Lee, I. H. El-Sayed, and M. A. El-Sayed, "Calculated absorption and scattering properties of gold nanoparticles of different size, shape, and composition: applications in biological imaging and biomedicine," *J. Phys. Chem. B* **110**(14), 7238–7248 (2006).
12. D. Huang, E. A. Swanson, C. P. Lin, J. S. Schuman, W. G. Stinson, W. Chang, M. R. Hee, T. Flotte, K. Gregory, and C. A. Puliafito, "Optical coherence tomography," *Science* **254**(5035), 1178–1181 (1991).
13. A. Fercher, C. Hitzenberger, G. Kamp, and S. El-Zaiat, "Measurement of intraocular distances by backscattering spectral interferometry," *Opt. Commun.* **117**(1-2), 43–48 (1995).
14. A. M. Gobin, M. H. Lee, N. J. Halas, W. D. James, R. A. Drezek, and J. L. West, "Near-infrared resonant nanoshells for combined optical imaging and photothermal cancer therapy," *Nano Lett.* **7**(7), 1929–1934 (2007).
15. M. Kirillin, M. Shirmanova, M. Sirotkina, M. Bugrova, B. Khlebtsov, and E. Zagaynova, "Contrasting properties of gold nanoshells and titanium dioxide nanoparticles for optical coherence tomography imaging of skin: Monte Carlo simulations and in vivo study," *J. Biomed. Opt.* **14**(2), 021017 (2009).
16. B. Vakoc, S. Yun, J. de Boer, G. Tearney, and B. Bouma, "Phase-resolved optical frequency domain imaging," *Opt. Express* **13**(14), 5483–5493 (2005).
17. A. L. Oldenburg, V. Crecea, S. A. Rinne, and S. A. Boppart, "Phase-resolved magnetomotive OCT for imaging nanomolar concentrations of magnetic nanoparticles in tissues," *Opt. Express* **16**(15), 11525–11539 (2008).
18. A. Oldenburg, F. Toublan, K. Suslick, A. Wei, and S. Boppart, "Magnetomotive contrast for in vivo optical coherence tomography," *Opt. Express* **13**(17), 6597–6614 (2005).
19. J. Oh, M. D. Feldman, J. Kim, H. W. Kang, P. Sanghi, and T. E. Milner, "Magneto-motive detection of tissue-based macrophages by differential phase optical coherence tomography," *Lasers Surg. Med.* **39**(3), 266–272 (2007).
20. D. C. Adler, S.-W. Huang, R. Huber, and J. G. Fujimoto, "Photothermal detection of gold nanoparticles using phase-sensitive optical coherence tomography," *Opt. Express* **16**(7), 4376–4393 (2008).
21. M. C. Skala, M. J. Crow, A. Wax, and J. A. Izatt, "Photothermal optical coherence tomography of epidermal growth factor receptor in live cells using immunotargeted gold nanospheres," *Nano Lett.* **8**(10), 3461–3467 (2008).
22. C. Zhou, T.-H. Tsai, D. C. Adler, H.-C. Lee, D. W. Cohen, A. Mondelblatt, Y. Wang, J. L. Connolly, and J. G. Fujimoto, "Photothermal optical coherence tomography in ex vivo human breast tissues using gold nanoshells," *Opt. Lett.* **35**(5), 700–702 (2010).
23. J. Kim, J. Oh, H. W. Kang, M. D. Feldman, and T. E. Milner, "Photothermal response of superparamagnetic iron oxide nanoparticles," *Lasers Surg. Med.* **40**(6), 415–421 (2008).
24. L. L. Ma, M. D. Feldman, J. M. Tam, A. S. Paranjape, K. K. Cheruku, T. A. Larson, J. O. Tam, D. R. Ingram, V. Paramita, J. W. Villard, J. T. Jenkins, T. Wang, G. D. Clarke, R. Asmis, K. Sokolov, B. Chandrasekar, T. E. Milner, and K. P. Johnston, "Small multifunctional nanoclusters (nanoroses) for targeted cellular imaging and therapy," *ACS Nano* **3**(9), 2686–2696 (2009).
25. M. Keijzer, R. R. Richards-Kortum, S. L. Jacques, and M. S. Feld, "Fluorescence spectroscopy of turbid media: Autofluorescence of the human aorta," *Appl. Opt.* **28**(20), 4286–4292 (1989).
26. S. Prah, "Mie Scattering Calculator", http://omlc.ogi.edu/calc/mie_calc.html.
27. F. Hyafil, J.-P. Laissy, M. Mazighi, D. Tchétché, L. Louedec, H. Adle-Biasette, S. Chillon, D. Henin, M.-P. Jacob, D. Letourneur, and L. J. Feldman, "Ferumoxtran-10-enhanced MRI of the hypercholesterolemic rabbit aorta: relationship between signal loss and macrophage infiltration," *Arterioscler. Thromb. Vasc. Biol.* **26**(1), 176–181 (2006).
28. Aurolate, www.Aurolate.com.
29. S. Yun, G. Tearney, J. de Boer, N. Iftimia, and B. Bouma, "High-speed optical frequency-domain imaging," *Opt. Express* **11**(22), 2953–2963 (2003).
30. R. Kuranov, A. McElroy, N. Kemp, S. Baranov, J. Taber, and T. Milner, "Gas-cell Referenced Swept Source Phase Sensitive Optical Coherence Tomography," *Opt. Technol. Lett.* (accepted).
31. M. Born, and E. Wolf, *Principles of Optics* (Cambridge University Press, Cambridge, 1999).
32. J. Kim, J. Oh, and T. E. Milner, "Measurement of optical path length change following pulsed laser irradiation using differential phase optical coherence tomography," *J. Biomed. Opt.* **11**(4), 041122 (2006).
33. B. C. Wilson, M. S. Patterson, and S. T. Flock, "Indirect versus direct techniques for the measurement of the optical properties of tissues," *Photochem. Photobiol.* **46**(5), 601–608 (1987).
34. M. V. Kunnnavakkam, F. M. Houlihan, M. Schlax, J. A. Liddle, P. Kolodner, O. Nalamasu, and J. A. Rogers, "Low-cost, low-loss microlens arrays fabricated by soft-lithography replication process," *Appl. Phys. Lett.* **82**(8), 1152–1154 (2003).
35. M. Varma-Nair, J. P. Wesson, and B. Wunderlich, "The thermal properties of polysiloxanes poly(dimethyl siloxane) and poly(diethyl siloxane)," *J. Therm. Anal. Calorim.* **35**(6), 1913–1939 (1989).
36. F. A. Duck, *Physical properties of tissue: a comprehensive reference book* (Academic Press, London New York 1990).

1. Introduction

Nanoparticles are finding increased application in the biomedical and clinical sciences for diagnostics [1] and therapeutics [2]. Although nanoparticles with various geometries and sizes have been synthesized and investigated in animal studies, interest has focused on particles less than 30-50nm in size because of improved targeting in part due to longer circulation times [3,4]. *In vivo* cellular imaging of tissues has emerged as a novel diagnostic tool in wide

ranging disciplines including ophthalmology, cardiology, and oncology [5–8]. Although early cellular imaging studies did not incorporate nanoparticles, later studies suggest that substantial contrast enhancement may be achieved using nanoparticles [9]. Optical properties of nanoparticles including absorption and scattering cross section have been computed using Mie theory [10] and the discrete dipole approximation [11]. Importantly these studies conclude that for nanoparticles in the clinically important range of 30-50nm, absorption dominates over scattering in contrast to larger sized particles in which scattering cross sections are relatively larger.

Currently, confocal microscopy imaging of tissues with nanoparticles for contrast enhancement is typically limited by a penetration depth of 200 microns or less which is insufficient for many diagnostic applications. To overcome this limitation, Huang et. al. [12] and Fercher et. al. [13] demonstrated a non-contact diagnostic method called optical coherence tomography (OCT). OCT provides a large penetration depth of up to 1-2 mm in tissues with a longitudinal spatial resolution of typically 10-15 μm . Gobin et. al. [14] demonstrated use of nanoparticles to enhance scattering contrast in OCT for detecting cellular targets in *in vivo* tissues. In this study, PEG enhanced gold nanoshells (143 nm diameter, core diameter 119nm) were injected intravascularly in tumor bearing mice and allowed to accumulate in malignant tissues passively through the leaky tumor vasculature. Backscattering of NIR light increased in dermal regions containing nanoparticles relative to controls where light was more strongly attenuated. Similarly, Kirillin et. al. [15] used gold nanoshells (75nm/25nm core radius/shell thickness) as enhanced contrast agents for intensity OCT imaging of porcine skin. Because the nanoparticles used in these studies were larger than 50nm, translation to *in vivo* clinical applications may be complicated by clearance concerns. Smaller particles permeate barriers more rapidly. Reducing nanoparticle size below 50nm for reduced clearance by the reticuloendothelial system is expected to render optical properties with absorption dominant to scattering and reducing OCT contrast [3].

In recent years, interest in phase sensitive OCT has increased [16]. In contrast to intensity OCT which measures only the intensity of backscattered light, phase sensitive OCT measures both the amplitude and phase of back scattered light. By measuring nanometer scale displacements in tissue in response to an external excitation, phase sensitive OCT provides additional functionality compared to intensity OCT, which is limited to micron resolution. Swept source phase-sensitive OCT achieves a high SNR (signal-to-noise ratio) and fast A-scan acquisition rates (up to 370 KHz) and allows detection of rapid changes in optical pathlength on the nanometer length scales in response to an external excitation. Oldenburg et al. [17,18] and Oh et. al [19] used phase sensitive OCT combined with an external magnetic field excitation to detect magnetic nanoparticles in tissue.

Photothermal OCT provides molecular contrast by combining phase sensitive OCT with laser excitation of targeted chromophores to measure optical pathlength (OP) variation. By targeting endogenous or exogenous (e.g. nanoparticles) chromophores by laser excitation, photothermal OCT can provide molecular contrast for clinical diagnostic imaging. Adler et al [20] have demonstrated use of photothermal OCT to measure optical pathlength (OP) variation in a translucent solution containing gold nanoshells (120 nm core, 16 nm) in response to 808nm excitation. In 2008, Skala et al [21] demonstrated use of depth resolved photothermal OCT to image OP variation due to gold nanospheres that absorb at 532 nm in a cell monolayer and three dimensional tissue constructs. In 2010, Zhou et.al [22]. demonstrated application of photothermal OCT to image *ex vivo* breast tissue containing injected gold nanoparticles. Kim et al. [23] demonstrated the use of a time-domain photothermal OCT system for detection of superparamagnetic iron oxide nanoparticles in a tissue phantom. Thus, previous studies have not made an attempt to estimate nanoparticle concentrations.

In this paper, we demonstrate a new method - depth resolved photothermal OCT—to detect and estimate concentration of nanoparticles in tissue phantoms and macrophage rich rabbit aortas. We use a novel magnetic nanoparticle cluster [20]—‘nanorose’ (~30nm in size)—that acts as an exogenous chromophore in tissue with a large absorption cross section in the NIR with the possibility of magnetic manipulation and imaging [24]. Because in the 30-

50nm range, nanoparticle absorption begins to dominate over scattering, utility of nanorose as an optical contrast agent for clinical diagnostics may be enhanced because photothermal OCT is based on absorption rather than scattering. We demonstrate here for the first time that depth resolved photothermal OCT can be used to detect and provide an estimate of nanoparticle concentration in scattering tissue phantoms and atherosclerotic rabbit aorta. We show experimentally that intravascular injection of nanorose combined with depth resolved photothermal OCT may be applied to detect macrophages that have engulfed nanorose in atherosclerotic *ex vivo* rabbit aorta.

2. Materials and methods

2.1 Nanorose

Novel clustered iron oxide/gold nanoparticles coated with dextran, we refer to as ‘nanorose’, were used as contrast agents [24]. The nanorose are spectrally tuned to give high absorption at 800nm and longer wavelengths in the near infrared. At 800nm, nanorose absorption cross section is substantially larger than the scattering cross section [24]. The 800nm laser excitation wavelength was selected for studies reported here to reduce absorption by competing endogenous chromophores in tissue (e.g., hemoglobin) while maximizing absorption by nanorose.

2.2 Tissue phantoms

Tissue phantoms were constructed from poly dimethyl siloxane (PDMS) and rutile TiO₂ as a scattering center with an average particle size of 1 micron. Absorption and scattering coefficients of the phantoms were matched to reported values for human aorta [25] by computing TiO₂ concentration using a Mie scattering calculator [26]. Phantoms with uniform thickness (250 μm) were prepared using a glass microscope slide as a substrate. Five types of tissue phantoms were prepared with variable nanorose concentration: 1) a control without nanorose; 2) 20ppm (ppm represents parts per million of gold concentration) giving a concentration of 6.4×10^9 nanorose/ml; 3) 10ppm giving a concentration of 3.2×10^9 nanorose/ml; 4) 1 ppm giving a concentration of 3.2×10^8 nanorose/ml; and 5) 0.1 ppm giving a concentration of 3.2×10^7 nanorose/ml.

2.3 Rabbit aorta

Fat-fed balloon injured New Zealand white rabbits [27] were used as an animal model of atherosclerosis for photothermal OCT measurements of nanorose injected intravenously and subsequently engulfed by plaque-based macrophages in response to 800nm laser excitation. All experimental procedures were performed in accordance with protocols approved by the University of Texas Institutional Animal Care and Use Committee. Macrophage-rich lesions were induced in New Zealand white rabbits by double balloon injury of the abdominal aorta and high cholesterol fat feeding as previously reported by Feldman and associates [27]. Briefly, following 2 ½ months of a high fat diet, and a protocol which included balloon de-endothelialization of the abdominal at 2 weeks, and balloon angioplasty of the abdominal aorta at 4 weeks, rabbits were ready for intravenous injection of the nanorose. New Zealand white rabbits (age = 6 months, weight = 3 kg, n = 3) were sedated with 2% isoflurane and 10cc of colloidal nanorose suspensions (1.4 mg Au / kg body weight) was injected intravenously into the ear veins. The administered gold dosage is approximately equal to the maximum currently allowed in humans by the United States FDA for treatment of rheumatoid arthritis [28]. Three days following nanorose injection, animals were euthanized with a lethal dose of sodium pentobarbital (120 mg/kg). Abdominal and thoracic aorta were removed, flushed with saline, and cut into 1x1 cm² square-sized specimens for photothermal OCT M-Mode imaging.

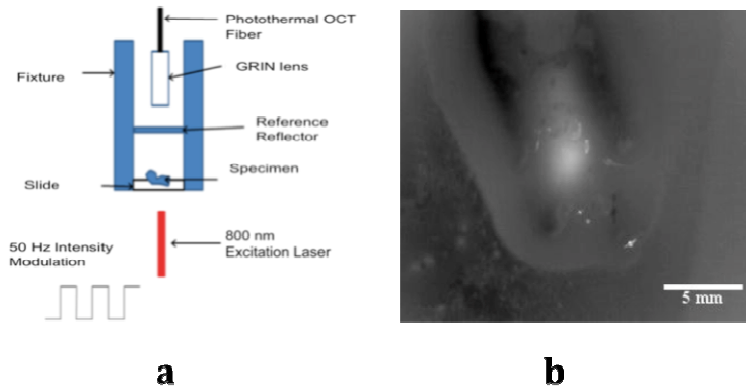


Fig. 1. (a). Diagram of photothermal OCT experimental setup. (b) Identification of “hot spot” in recorded infrared image

2.4 Photothermal OCT measurements

2.4.1 Photothermal OCT system

We designed and constructed a swept source photothermal OCT system that uses a hydrogen-fluoride gas-cell to trigger A-scan acquisitions. The tunable swept-source laser has emission centered at 1328nm with a bandwidth of 100nm and a 20kHz A-scan rate (Santec HSL-10000). The axial coherence length of the system is 21 microns in air. A real-time external clock eliminated requirement for post-acquisition interpolation of spectral fringe data [29]. We designed and developed real-time acquisition software, which allows display of acquired M-mode images at video rates (up to 100Hz). Additional specifications of the system are described elsewhere [30].

The photothermal OCT experimental setup [Fig. 1(a)] used a customized fixture designed to minimize random phase variations from the environment and maintain the sample holder in a mechanically fixed position relative to the reference surface. The photothermal OCT beam is incident on the specimen from the top and records M-mode images of optical pathlength (OP) variation in the specimen in response to laser (800 nm) excitation. An 800nm diode laser co-aligned and oppositely directed to the OCT beam was used to excite the specimen. Laser excitation was set at 2W and intensity-modulated ($f_i = 50\text{Hz}$) with a duty cycle of 50%. The laser excitation spot diameter on the back surface of the tissue specimen was fixed at 2mm giving an incidence fluence rate of $64\text{W}/\text{cm}^2$.

2.4.2 Tissue phantom photothermal OCT measurements

Tissue phantoms were inserted into the fixture, irradiated with intensity-modulated ($f_i = 50\text{Hz}$) laser (800nm) light and photothermal OCT M-mode images recorded. Tissue phantoms were irradiated for 5 seconds and photothermal OCT M-mode images were recorded at an A-scan rate of 20kHz with a fringe data sampling rate of approximately 20MS/s. Photothermal OCT M-Mode images consist of 100,000 successive A-scans recorded over a five-second time period without translating the OCT beam on the specimen. Surface ($z = 0$) and depth-resolved optical pathlength (OP) variation ($\delta(z,t)$) was computed from recorded photothermal OCT M-mode images using customized software developed in our laboratory. Optical depth (z) is the product of refractive index and physical depth [31]. OP ($\delta(z,t)$) is the time-resolved variation in optical depth (z) in the specimen. Surface and depth-resolved peak-to-peak optical pathlength modulation amplitude (OPMA, $(\delta(z,f_i))$) was computed from recorded photothermal OCT M-mode images. OPMA was determined from the fast Fourier transform of the OP variation at the laser (800nm) modulation frequency (f_i). OPMA is the peak-to-peak variation in optical pathlength at the laser excitation frequency ($f_i = 50\text{ Hz}$) at optical depth z and

averaged over the photothermal OCT M-mode acquisition period and is referenced as $(\delta(z, f_i))$ in the following discussion.

2.4.3 Rabbit aorta photothermal OCT measurements

In photothermal OCT M-mode imaging of macrophage-rich rabbit abdominal aorta, a preliminary step involved identifying candidate regions for imaging that had taken up nanorose. To identify candidate regions for photothermal OCT imaging, the aorta tissue sections were irradiated with 800nm laser excitation light from the adventitial side with an infrared camera (FLIR SC4000) viewing the intima surface. Regions with increased infrared radiometric temperature in response to 800nm laser excitation light were identified as “hot spots” in recorded images [Fig. 1(b)]. Hot spot locations were identified and the specimens were positioned in the photothermal OCT setup for M-mode imaging. Care was exercised to ensure relative position of the tissue specimen and 800nm laser excitation light was unchanged for infrared imaging and photothermal OCT M-mode imaging. The non-balloon injured thoracic aorta served as the control for each rabbit and were imaged using infrared and photothermal OCT in a similar manner as the macrophage-rich abdominal aorta. Prior to recording M-mode images, the photothermal OCT beam was focused to a 20- μm spot at approximately 200- μm under the air-tissue interface. The 800nm laser excitation beam (2mm spot diameter) was oppositely directed and co-registered to the photothermal OCT probe beam [Fig. 1(a)]. Tissue specimens were irradiated by intensity-modulated (50 Hz, 50% duty cycle, 2W average power) 800 nm laser light over a two-second time period while photothermal OCT M-mode images consisting of 40,000 A-scans were recorded. In both infrared and photothermal OCT M-mode imaging experiments, maximum radiometric temperature was maintained below 30°C to avoid protein denaturation and dehydration. After photothermal OCT M-mode imaging, OP $(\delta(z, t))$ variation and OPMA $(\delta(z, f_i))$ were computed and tissue specimens were placed in formalin and processed for histology.

2.5 Histological analysis and fluorescence imaging

Processed tissue specimens were cut into 5 μm thick sections and stained with hematoxylin and eosin for general structure identification and RAM-11 (Dako Anti-Rabbit Macrophage Clone RAM11) for macrophage cell identification. Paired sections were prepared for darkfield microscopy to detect the presence of nanorose. Tissue sections were imaged with light microscopy using a Leica DM6000 upright light microscope fitted with a Spot IDEA digitizing camera coupled to a computer with image acquisition software. Brightfield images were captured and recorded for adjacent sections stained with hematoxylin and eosin and RAM 11. Darkfield microscopy was similarly performed after substituting a Zeiss X278 darkfield condenser for the brightfield condenser. To take advantage of difference in optical properties between nanorose and native aortic plaque components, a 610 nm long pass filter was positioned in the imaging path of the microscope to attenuate reflected light with wavelengths shorter than 610 nm.

3. Results

3.1 Tissue phantom photothermal OCT measurements

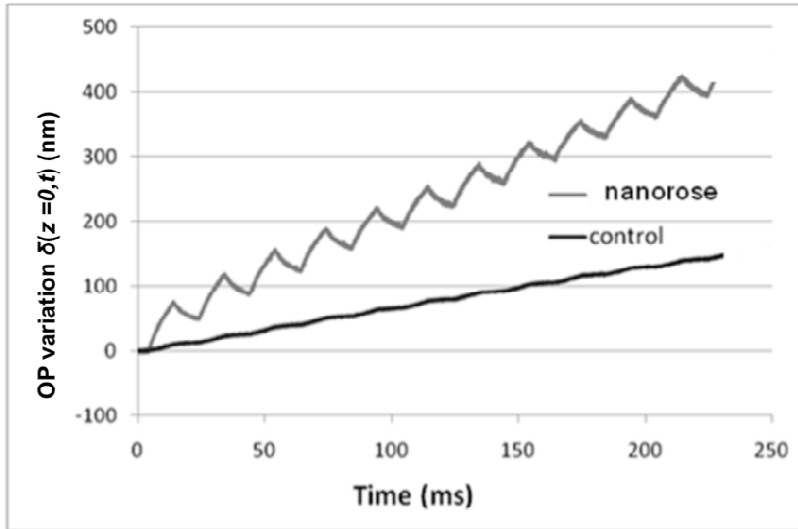


Fig. 2. OP variation ($\delta(z=0,t)$) of the air-phantom interface of control (black) and nanorose (grey) tissue phantom (6.3×10^9 nanoroses/ml) measured by photothermal OCT in response to intensity-modulated ($f_i = 50$ Hz) laser (800nm) excitation.

3.1.1 Phantom photothermal OCT surface measurements

OP variation ($\delta(z,t)$) of the air-phantom interface ($z = 0$) in the control and tissue phantoms containing nanorose were computed from recorded photothermal OCT M-mode images (Fig. 2). Phantoms containing nanorose exhibit greater OP variation ($\delta(z=0,t)$) than the control phantom (without nanorose) in response to laser (800nm) excitation. Plot of OP variation vs. time (Fig. 2) indicates a distinct 50 Hz oscillation is observed in nanorose phantoms that is not evident in controls.

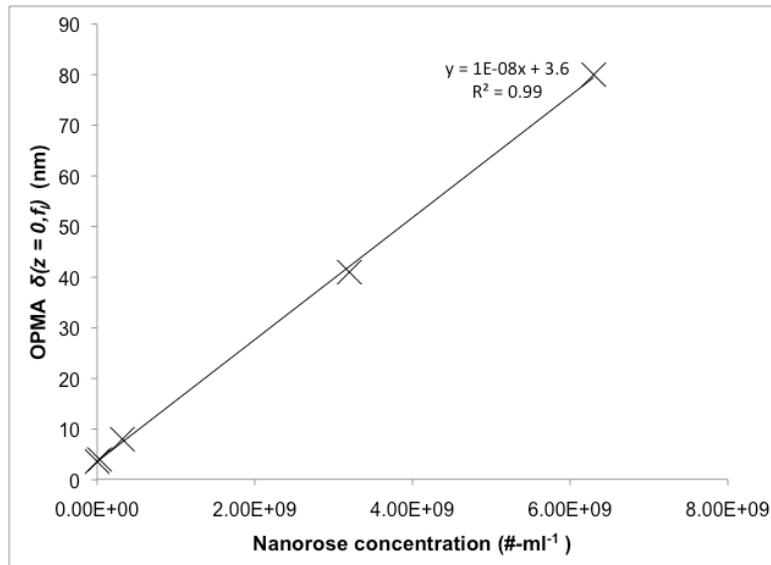


Fig. 3. OPMA ($\delta(z = 0, f_i)$) of the air-phantom interface vs. nanorose concentration computed from photothermal OCT M-mode images in response to intensity-modulated ($f_i = 50$ Hz) laser (800nm) excitation (\times). Solid line is linear least squares fit.

Experiments were performed with tissue phantoms containing nanorose at various concentrations: 6.4×10^9 nanoroses/ml, 3.2×10^9 nanoroses/ml, 3.2×10^8 nanoroses/ml and 3.2×10^7 nanoroses/ml. OPMA ($\delta(z = 0, f_i)$) at the air-phantom interface was computed from recorded photothermal OCT M-mode images. Greatest OPMA (80 nm) at the air-phantom interface ($z = 0$) was observed in the tissue phantom with greatest nanorose concentration (6.4×10^9 nanoroses/ml). Tissue phantom with a concentration of 3.2×10^9 nanorose/ml showed a 40nm OPMA at the air-phantom interface ($z = 0$). Tissue phantom with a concentration of 3.2×10^8 nanoroses/ml showed an OPMA of 8nm while the phantom with 3.2×10^7 nanoroses/ml showed an OPMA of 4nm at the air-phantom interface ($z = 0$). OPMA of the air-phantom interface ($z = 0$) versus nanorose concentration (Fig. 3) suggests a linear relationship exists between OPMA at the air-phantom interface ($z = 0$) and nanorose concentration. A linear least squares fit indicates slope of the trend line is 1.0×10^{-8} nm·ml and an intercept of 3.6 nm. Radiometric temperature increase of tissue phantoms in response to one modulation cycle of 800nm laser excitation was less than 0.064° C.

3.1.2 Phantom photothermal OCT depth resolved measurements

Depth resolved OPMA ($\delta(z, f_i)$) vs. optical depth (Fig. 4) in response to intensity-modulated ($f_i = 50$ Hz) laser (800 nm) excitation was recorded from four tissue phantoms containing variable nanorose concentrations (6.4×10^9 nanoroses/ml; 3.2×10^9 nanoroses/ml; 3.2×10^8 nanoroses/ml). The tissue phantom with lowest nanorose concentration (3.2×10^7 nanoroses/ml) showed a negligible depth resolved OPMA and was not included our analysis.

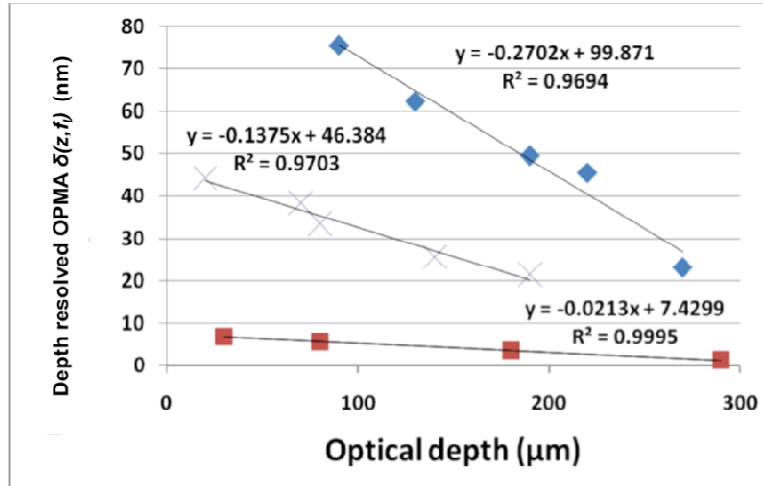


Fig. 4. Depth resolved OPMA ($\delta(z, f_i)$) vs. optical depth (z) in tissue phantoms with variable nanorose concentration in response to intensity-modulated ($f_i = 50$ Hz) laser (800nm) excitation (◆ - 6.4×10^9 nanoroses/ml; × - 3.2×10^9 nanoroses/ml; ■ - 3.2×10^8 nanoroses/ml)

3.2 Rabbit aorta experiments

3.2.1 Rabbit aorta photothermal OCT surface measurements

We tested the ability of photothermal OCT to detect nanorose in response to laser excitation in macrophage-rich abdominal and macrophage-poor thoracic (paired control) aorta specimens. OPMA ($\delta(z, f_i)$) at the surface ($z = 0$) was computed from recorded photothermal OCT M-Mode images of macrophage-rich and control rabbit aorta specimens. Depth resolved OPMA ($\delta(z, f_i)$) was also computed and is described in the next section. OPMA ($\delta(z, f_i)$) at the surface ($z = 0$) of macrophage-rich abdominal aorta containing nanorose is approximately five-fold larger than that in controls (Fig. 5).

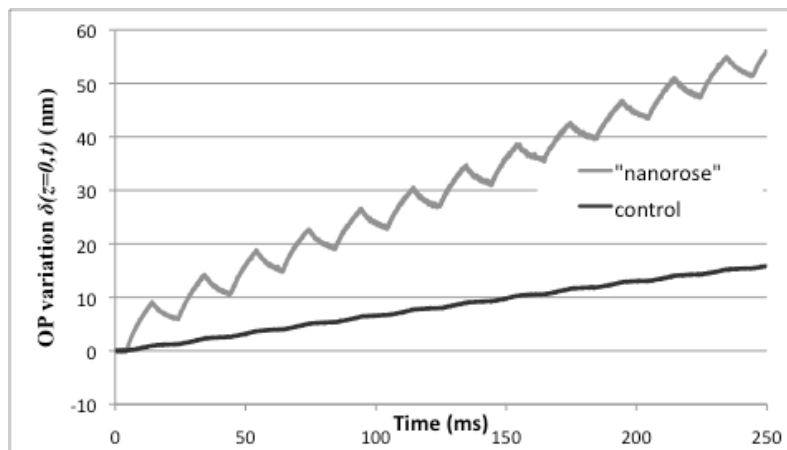


Fig. 5. OP ($\delta(z = 0, t)$) variation at the surface ($z = 0$) in macrophage-rich and control rabbit aorta specimens.

OP variation ($\delta(z = 0, t)$) of the air-tissue interface ($z = 0$) of macrophage-rich and control rabbit aorta was computed from recorded photothermal OCT M-mode images (Fig. 5). OP variation shows a distinct 50 Hz oscillation in the macrophage-rich abdominal aortic sample that is smaller in control thoracic aorta. The macrophage-rich abdominal rabbit aorta with

engulfed nanorose showed an average OPMA of $\delta(z = 0, f_i) = 10\text{nm}$. The control thoracic rabbit aorta showed an average OPMA of $\delta(z = 0, f_i) = 3\text{nm}$.

3.2.2 Rabbit aorta depth resolved photothermal OCT measurements

Depth resolved OPMA in response to laser (800 nm) excitation recorded from macrophage-rich and control rabbit aorta specimens was calculated from recorded photothermal OCT M-mode images. Figure 6 demonstrates OPMA ($\delta(z, f_i)$) vs. optical depth from macrophage-rich and control specimens (A: Abdominal (macrophage-rich) and T: Thoracic (control)). OPMA magnitude and slope is distinctively different for macrophage-rich versus control specimens. Magnitude of OPMA in macrophage-rich abdominal aorta tissue specimens is 2.5-5.0x larger than in control thoracic aorta specimens. For macrophage-rich abdominal aorta tissue specimens, slope of $\delta(z, f_i)$ is reduced and OPMA does not decrease significantly (<15%) with increasing depth (Fig. 6). In comparison, in control thoracic aorta specimens, slope of $\delta(z, f_i)$ is more negative and OPMA shows a more rapid decrease (more than 70%) with increasing optical depth (Fig. 6). At the deepest optical depths ($z = 400\mu\text{m}$), OPMA of macrophage-rich abdominal aorta specimens is 5X larger than that in control thoracic tissues. Observed differences in magnitude and slope of $\delta(z, f_i)$ suggests that depth-resolved photothermal response is distinctly different between macrophage-rich and control aortas.

Statistical differences in OPMA (nm) versus optical depth (mm) of macrophage-rich and control rabbit aortas were performed (Fig. 6). A two-sided test with a significance level of 5% and predicted values estimated based on a repeated measures linear model in terms of location, optical depth, and the optical depth by location interaction with an autoregressive order-one correlation assumption [SAS Version 9.1 for Windows, SAS Institute, Cary, North Carolina]. For each anatomical location, whiskers extend to the predicted value plus or minus one standard error [Abdomen: Black, Thorax: Red]. The location effect ($p = 0.002$) and optical depth by location interaction ($p = 0.03$) were significant indicating a statistically significant difference between macrophage-rich and control aorta with optical depth in both mean OPMA and OPMA slope.

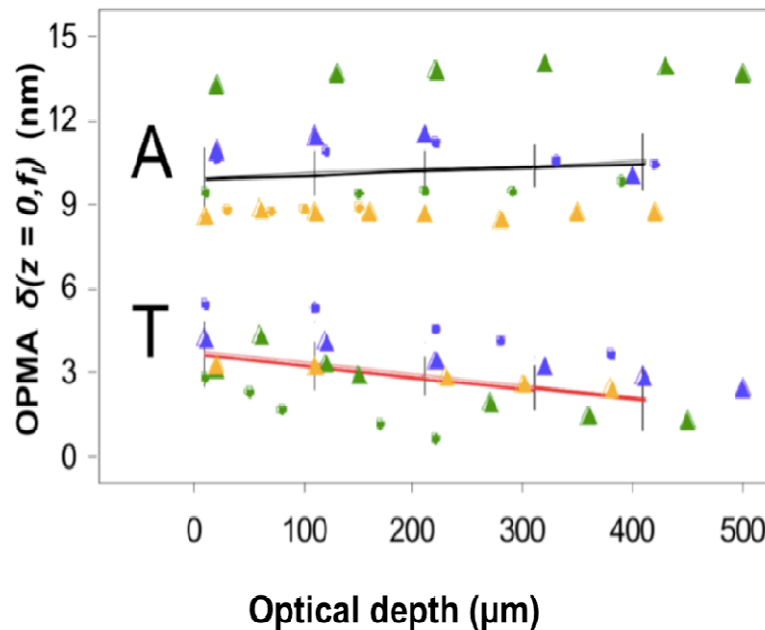


Fig. 6. Replicate OPMA (nm) and optical depth (microns) measurements in three rabbits measured in each of two anatomical locations [A: Abdomen (injured), T: Thorax (control)] at up to six different depths. Animals are identified by color (blue, green, orange) and replicates by symbol (triangle, dot).

3.3 Histological results

Histological images of macrophage-rich tissue sections from a double balloon-injured, fat fed New Zealand white rabbit injected 3 days before sacrifice with intravascular nanorose at a dose of 1.4mg Au/kg body weight confirms an area rich in macrophages in the intimal hyperplasia by positive RAM 11 (brown color) stain (Fig. 7). A lack of RAM 11 stain, and thus an absence of macrophages, is observed in the control. Nanorose are identified in 610 nm longpass-filtered darkfield microscopy images as bright red reflections on a dark background. The relative absence of highly-reflective constituents compared to control and macrophage-rich tissue sections coupled with enhanced reflectivity of nanorose at wavelengths longer than 610nm is responsible for bright areas observed in darkfield microscopy images. In Fig. 7, images of macrophage-rich tissue sections are positive for nanorose while the control tissue is negative. Taken together with RAM 11 results, microscopy images suggest that macrophage-rich abdominal aorta tissues contain nanoroses, while the control thoracic aorta specimens contain neither macrophages nor nanorose.

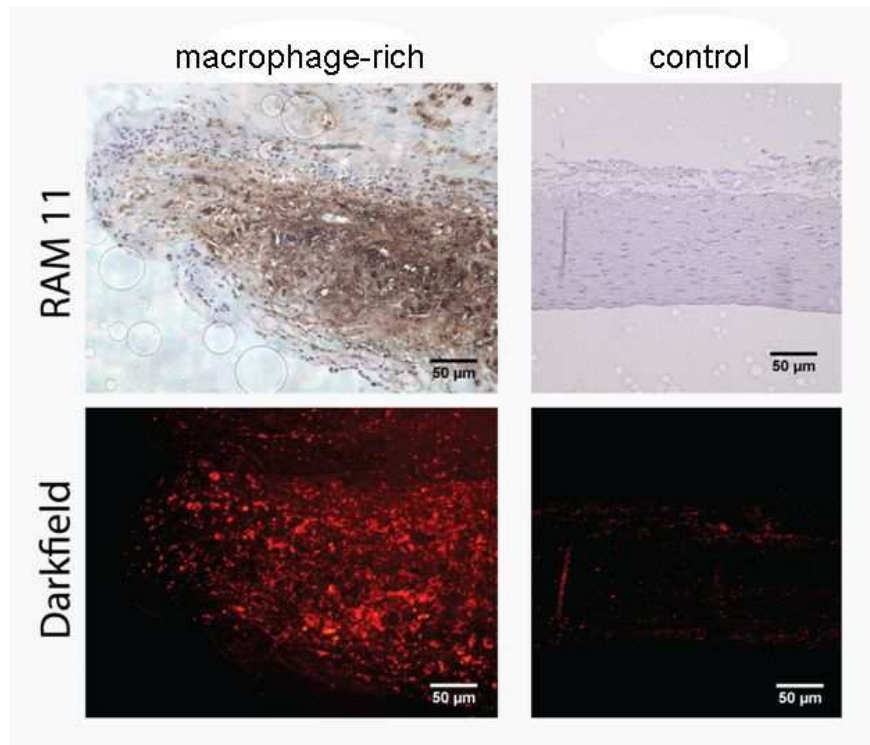


Fig. 7. Microscopy images of macrophage-rich and control sections. Macrophage-rich abdominal (left column) and control thoracic aorta (right column); Brightfield RAM-11 stained (top Row) and darkfield (bottom row) unstained microscopy images. Scale bar = 50 microns.

4. Discussion

4.1 Tissue phantom photothermal OCT measurements

From recorded photothermal OCT M-mode images of tissue phantoms we computed OPMA at the air-phantom interface ($z = 0$) and depth resolved variation for increasing nanorose concentrations. We present analytical models of both surface and depth-resolved OPMA measurements and interpret our results.

4.1.1 Tissue phantom photothermal OCT surface measurements

A linear relationship is observed (Fig. 3) between OPMA of the air-phantom interface and nanorose concentration. Slope of the line is related to nanorose concentration while a non-negative y-intercept suggests that PDMS phantoms exhibit some residual absorption without any nanorose. The result supports our hypothesis that thermoelastic expansion is caused in large part by the selective absorption of incident laser (800nm) radiation by nanorose. Kim et al. [32] presented an algebraic expression for the one-dimensional thermoelastic displacement of a laser heated specimen. OPMA at the air-phantom interface is given by Eq. (1).

$$\delta(z = l_0, f_i) = \frac{\alpha(1+\nu)}{3(1-\nu)} \int_{z_1}^{z_2} \Delta T_{if}(z) \cdot dz \quad (1)$$

where α is thermoelastic expansion, ν is Poisson's ratio and $\delta(z = l_0, f_i)$ is the OPMA at the air-phantom interface (Fig. 6). In this equation, the phantom is on a glass slide with position of the glass-phantom interface at $z = 0$. Phantom thickness is given by l_0 while the air-phantom interface is at $z = l_0$. The temperature increase (ΔT_{if}) in the phantom over one modulation cycle of 800nm laser excitation is given by Eq. (2):

$$\Delta T_{if}(z) = \frac{\sigma N \phi(z)}{2\rho C f_i} + \frac{\mu_{PDMS} \phi(z)}{2\rho C f_i} \quad (2)$$

where $\Delta T_{if}(z)$ is the depth-resolved temperature rise over one modulation cycle of laser excitation, σ is the nanorose absorption cross section, N is nanorose concentration, $\Phi(z)$ is depth resolved optical fluence rate, ρC is the volumetric heat capacity of PDMS, and μ_{PDMS} is the absorption coefficient of PDMS without nanorose. Monte Carlo simulations were performed to assess the depth-dependence (z) of optical fluence rate ($\Phi(z)$) and suggest that for thin phantoms (250 microns) used in our experiments, the optical fluence rate (Φ) is nearly constant in depth (z). Taking into account the above assumptions OPMA at the air-phantom interface is given by

$$\delta(z = l_0, f_i) = \frac{\alpha(1+\nu)\sigma\phi l_0}{6(1-\nu)\rho C f_i} \cdot N + \frac{\alpha(1+\nu)\mu_{PDMS}\phi l_0}{6(1-\nu)\rho C f_i} \quad (3)$$

Substituting a Poisson's ratio of $\nu = 0.5$, predicted slope ($\frac{d\delta}{dN}$) of the best-fit line in Fig. 3 is given by Eq. (4).

$$\frac{d\delta}{dN} = \frac{\alpha\sigma\phi l_0}{2\rho C f_i} \quad (4)$$

where f_i is the frequency of laser intensity modulation. The absorption cross section ($\sigma = 3.1 \pm 0.5 \times 10^{-14} \text{ m}^2$) of the nanoparticles was measured using an approach employing an integrating sphere [33]. The laser spot size was measured using a knife edge test and the resultant optical fluence rate (Φ) of 64 W/cm^2 was estimated. Thermoelastic expansion coefficient (α) of the PDMS is $310 \text{ ppm/}^\circ\text{C}$ [34] and phantoms were $l_0 = 250$ microns thick. The volumetric heat capacity (ρC) of PDMS was taken as $1447.5 \times 10^3 \text{ J/(m}^3\text{K)}$ [35].

Using Eq. (4), values specified above and accounting for uncertainty of the measured nanorose absorption cross section, computed OPMA at the air-phantom interface per unit nanorose concentration is $\frac{d\delta}{dN} = 1.05 \pm 0.25 \cdot 10^{-8} \text{ nm-ml}$. From the plot in Fig. 3, slope of the best fit line is $1.0 \times 10^{-8} \text{ nm-ml}$. Computed OPMA at the air-phantom interface per unit nanorose concentration values deduced from Eq. (4) ($1.05 \pm 0.25 \cdot 10^{-8} \text{ nm-ml}$) and experiment ($1.0 \times 10^{-8} \text{ nm-ml}$) are consistent within experimental error of the nanorose absorption cross section measurement.

4.1.2 Tissue phantom photothermal OCT depth resolved measurements

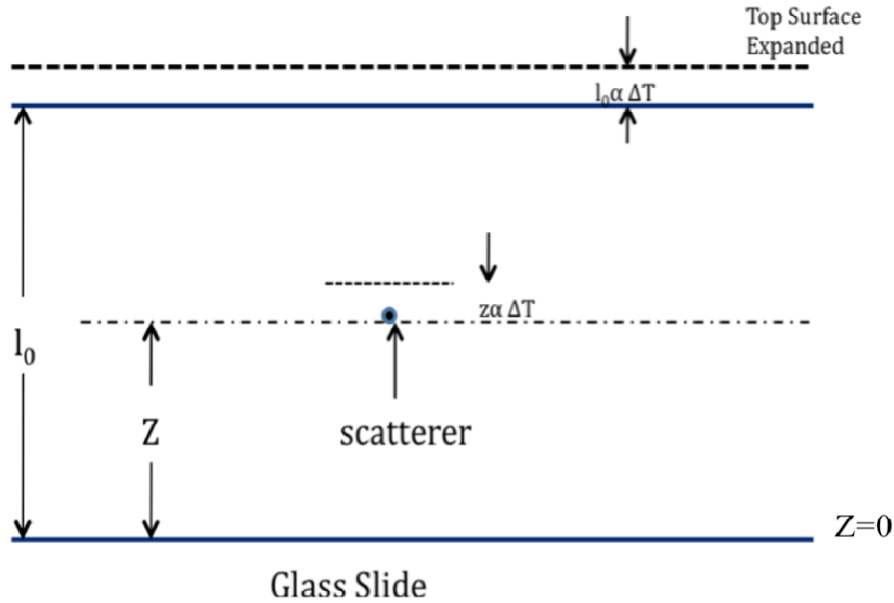


Fig. 8. Phantom and scatterer

Figure 8 shows a cartoon of the tissue phantom with thickness (l_0) on a glass slide substrate with a scattering center positioned at a distance ‘ z ’ above the glass-phantom interface. When laser light is absorbed and heats the phantom, OP variation occurs. For a scattering center at a distance z above the glass-phantom interface, the change in OP of light backscattered from the scattering center as a result of a temperature increase (ΔT) is given by,

$$\delta(z, f_l) = [(n_0 - 1) \alpha l_0 + l_0 \frac{\delta n}{\delta T} - z (n_o \alpha + \frac{\delta n}{\delta T})] \Delta T \quad (5)$$

Where ΔT is given by Eq. (2) with $\Phi(z) = \Phi_o$. Eq. (5) is derived by considering change in OP due to thermoelastic expansion and change of the refractive index due to temperature ($\frac{\delta n}{\delta T}$). In Eq. (5), $\delta > 0$ ($\delta < 0$) indicates an increase (decrease) in optical pathlength. At the air-phantom interface ($z = l_o$) Eq. (5) simplifies to the well-known result,

$$\delta(z = l_o, f_l) = -l_o \alpha \Delta T \quad (6)$$

For a positive temperature increase ($\Delta T > 0$), change in OP ($\delta(z = l_o, f_l)$) is negative indicating a reduced optical pathlength. Depth-resolved OPMA of tissue phantoms was computed and plotted (Fig. 4). Slope of fitted lines (Fig. 4) provide measured values of OPMA per unit depth. To calculate the predicted value of OPMA per unit depth, Eq. (5) was used. In the first step, the value of $(n_o \alpha + \frac{\delta n}{\delta T})$ was calculated as 3.37×10^{-4} . The surface displacement corresponding to different nanorose concentrations and the value of $(n_o \alpha + \frac{\delta n}{\delta T})$, were then used to calculate the expected temperature increase in the phantoms over one cycle of laser excitation. Using the value of $(n_o \alpha + \frac{\delta n}{\delta T})$ and the actual temperature rise, the OPMA per unit optical depth was calculated from Eq. (5) and a measured value of

OPMA per unit optical depth was obtained from Fig. 4. Table 1 shows the measured and calculated value of OPMA per unit depth for different phantoms.

Table 1. OPMA per unit depth (calculated and measured) for different concentrations

Concentration of nanoparticles in phantom (nanorose/ml)	OPMA per unit optical depth (calculated nm/mm)	OPMA per unit optical depth (measured nm/mm)
6.4×10^9	0.25	0.27
3.2×10^9	0.15	0.14
3.2×10^8	0.02	0.02

4.2 Rabbit aorta tissue photothermal OCT measurements

4.2.1 Rabbit aorta tissue photothermal OCT surface measurements

Figure 7 and results described in section 3.2.1 suggest that nanoparticles were selectively engulfed by macrophage rich abdominal rabbit aorta. Determining the nanorose concentration in aorta sections could be of significant clinical interest for nanoparticle dosimetry studies, where the greater the macrophage density, the more vulnerable the plaque is to rupture resulting in clinical events. Macrophage rich abdominal aorta sections exhibit an OPMA (9-12nm) and control thoracic aorta sections exhibit a smaller OPMA (2-3 nm) at the air-tissue interface. The OPMA due to nanorose is taken as the difference between abdominal and control OPMA. To estimate the concentration of nanoparticles in the abdominal aorta section, we use the OPMA model presented in section 4.1.1. Several assumptions were made in deriving this equation, namely a uniform optical fluence, a uniform sample thickness, uniform volumetric heat capacity, and a uniform spatial distribution of nanoparticles. Also thickness of the phantoms was 250 μm while the histology studies indicated that nanoparticle layers in aorta were about 200 μm . To estimate nanorose concentration in tissue, we scale the slope measured in phantoms (0.8×10^{-8} nm-ml) to account for different thicknesses between nanorose in tissue and phantoms. In absence of reliable values for the coefficient of thermal expansion and volumetric heat capacity of aorta, values for cardiac muscle of rabbit [36] were used and an estimate of OPMA per unit concentration of nanoparticles in aortic tissue was estimated as 4.32×10^{-9} nm-ml. Accounting for all the simplifying assumptions, and using the measured OPMA in macrophage-rich and control aorta specimens and the extrapolated OPMA per unit concentration of nanoparticles, for the first time localized nanorose concentration can be estimated at the probed site in the macrophage-rich abdominal aorta sections as 8ppm (2.5×10^9 particles/ml).

4.2.2 Rabbit aorta tissue photothermal OCT depth resolved measurements

OPMA of control thoracic aortas (Fig. 6) is observed to decrease with increasing depth (z). The observed decrease in OPMA ($\delta(z, f_i)$) with increasing optical depth (z) is similar to that observed in tissue phantoms with a uniform absorption profile. Histology of control thoracic aortas did not exhibit a high concentration of macrophages. Inasmuch as aortic tissue can absorb 800nm light, some component of OPMA is due to absorption by endogenous chromophores as was observed in experiments with tissue phantoms. Because the control thoracic aortic tissue is believed to absorb laser light (800 nm) homogenously, OPMA is expected to decrease linearly with increasing depth as observed in experiments with tissue phantoms.

OPMA of macrophage-rich aortas (Fig. 6) is not observed to decrease significantly with increasing depth (z). The flat OPMA profile observed in macrophage-rich abdominal aorta tissues suggests a non-uniform distribution of nanoroses may be present. Moreover, significant OPMA is observed at optical depths as deep as 400 μm in aorta sections.

Nanoroses can enter the aortic wall either through the lumen or vasa vasorum. When nanorose enter through the lumen, we expect an increased concentration of nanoparticles near the luminal surface. When nanorose enter through the vasa vasorum, we expect increased

concentration of nanoparticles near the outer vessel wall. Based on these two delivery pathways, we expect and the histology demonstrates that deposition of nanorose in abdominal aorta can exhibit a non-uniform distribution. The flat OPMA vs. depth (z) profile may be due to presence of nanorose at deeper depths that are delivered through the vasa vasorum. Further, the deposition of the macrophages is not homogenous but is variable, which can also contribute to the non-uniform distribution of the nanorose.

In the rabbit aorta and tissue phantom experiments, we assumed a constant optical fluence distribution. However, in practice, the fluence in tissue is not uniform and will need to be examined to analyze depth-resolved OPMA measurements in macrophage-rich aorta. We assumed a uniform volumetric heat capacity for phantoms and aorta. This assumption is an oversimplification since the volumetric heat capacity of tissues can change with tissue constituents. Particularly, the volumetric heat capacity can have a strong dependence on the lipid concentration. Photothermal OCT requires the selection of an excitation laser of appropriate wavelength to excite target chromophores. However, because the distribution of chromophores is not uniform in tissue, our models of depth-resolved OPMA require some generalization for non-uniform nanorose distributions before applying to macrophage-rich abdominal aorta.

We have demonstrated that by using photothermal OCT, depth-resolved OP variation may be measured for the first time in *ex vivo* tissue preparations, and we derived a relationship between OP and nanorose concentration. Knowledge of the correlation between nanorose concentration and OPMA can be used to develop a method to estimate nanorose concentration in macrophages, which is of interest since vulnerable plaques known to rupture and result in clinical events have greater density of macrophages. However, development of such an approach requires further experimentation and development. First, experiments must be performed on phantoms with a non-uniform distribution of nanorose. Second, an imaging equation that generalizes the result given in Eq. (6) must be developed for the case when nanorose concentration may vary with depth. Third, finding a solution to this imaging equation from recorded photothermal OCT measurements may allow determination of the concentration profile of a targeted chromophore (e.g. nanorose).

5. Conclusions

We present for the first time both surface and depth-resolved OP variation measurements using photothermal OCT in tissues and phantoms containing nanoroses and a quantitative interpretation of the results. Using photothermal OCT and 'nanorose' with a size between 30 and 50nm, nanoparticle absorption begins to dominate over scattering. Because photothermal OCT is based on absorption rather than scattering the approach described may allow use of nanorose as an optical contrast agent for clinical diagnostics. Tissue phantoms containing nanorose exhibited greater thermoelastic displacement than that observed in controls without nanorose. Values of OP variation measured using photothermal OCT per unit nanorose concentration deduced from experiment are in quantitative agreement with predicted values. The *ex vivo* rabbit aorta exhibited a similar trend to that observed in tissue phantoms. Aortic tissue with engulfed nanorose (abdominal aorta) exhibited a statistically greater OP variation as compared to aortic tissue sections containing fewer nanoroses (thoracic aorta). We conclude that atherosclerotic aortic regions with increased OPMA for incident 800nm laser excitation may be attributed to specific targeting of nanoroses of macrophage cells associated with plaque and nanorose concentration may be non-uniform. Further studies are required to develop an approach to estimate depth profile of nanorose concentration from recorded photothermal OCT measurements.

Acknowledgements

The authors gratefully acknowledge the Veterans Administration and the National Institutes of Health (R01EY016462-04) for financial support to this research.